Article

Synthesis and Characterization of a Photocatalytic Material from TiO₂ Nanoparticles Supported on Zeolite Obtained from Ignimbrite Residue Used in Decolorization of Methyl Orange

Gianina Huayna [1], **Antonio Laura** [1], **Rossibel Churata** [1], **Luis Lazo** [1], **Rivalino Guzmán** [1,*], **Pierre G. Ramos** [2] **and Juan M. Rodriguez** [2]

[1] Universidad Nacional de San Agustín de Arequipa UNSA, Av. Independencia s/n, Arequipa 04001, Peru; ghuayna@unsa.edu.pe (G.H.); alauraqu@unsa.edu.pe (A.L.); rchurataa@unsa.edu.pe (R.C.); llazoal@unsa.edu.pe (L.L.)

[2] Center for the Development of Advanced Materials and Nanotechnology, Universidad Nacional de Ingeniería, Av. Túpac Amaru 210, Lima 15333, Peru; pierreramos1990@gmail.com (P.G.R.); jrodriguez@uni.edu.pe (J.M.R.)

* Correspondence: rguzmana@unsa.edu.pe; Tel.: +51-9-3027-5495

Abstract: In the present work, a TiO₂/zeolite photocatalyst was synthesized by dispersing TiO₂ nanoparticles obtained through the sol-gel method onto the surface of natural zeolite derived from ignimbrite residue. The zeolite was obtained from an ignimbrite rubble treatment collected from a quarry in Arequipa City, Peru. The research focused on the effect of zeolite on the TiO₂ nanoparticles. The synthesized photocatalysts were characterized using various techniques, including field-emission scanning electron microscopy (FE-SEM), energy-dispersive X-ray (EDS), X-ray diffraction (XRD), diffuse reflectance spectroscopy (DRS), and Brunauer–Emmett–Teller surface area analysis (BET). The results revealed that the TiO₂/zeolite samples displayed high crystallinity, with TiO₂ being present in three phases and zeolite being present in the analcime phase. Furthermore, these samples exhibited a band gap of 3.14 eV and a high surface area compared to that of bare TiO₂. Finally, the photocatalytic activity of the TiO₂/zeolite composite obtained was evaluated toward the decomposition of 10 ppm and 20 ppm of methyl orange (MO) dye. The TiO₂/zeolite samples demonstrated improved photocatalytic activity compared to that of pristine TiO₂ under the same experimental conditions. This enhancement is primarily attributed to the increased specific surface area of the TiO₂/zeolite samples, making them promising materials for future efficient and sustainable photocatalytic applications.

Keywords: titanium dioxide; analcime zeolite; ignimbrite; photocatalysis; nanomaterial

1. Introduction

Water pollutants, including detergents, industrial chemicals, pesticides, and organic dyes, pose significant environmental threats. These substances are produced by diverse industries [1,2], such as the food, textile, cosmetics, paper, and other sectors [3]. Consequently, efforts have been concentrated on exploring innovative materials and developing efficient wastewater treatment methods to address this environmental concern. Several techniques have been studied for their effectiveness, including adsorption, ion exchange, chemical oxidation, electrolysis, and photocatalytic treatments [4,5].

In recent years, photocatalysis has emerged as a promising and eco-friendly technology. This simple yet potent method has shown a high potential for reducing organic pollution by facilitating an absolute decrease in toxic substances [6]. Several photocatalyst materials have been described, such as ZnO, CuO, TiO₂, WO₃, Fe₂O₃, and CuO [7–9]; among them, titanium dioxide (TiO₂) stands out, especially due to its properties such as low cost, nontoxicity, and high stability in aqueous media and its safe handling [10,11]. However, the high aggregation tendency, low adsorption capacity, and difficult recovery of TiO₂ limit

its application in water treatment [12,13]; therefore, many researchers have focused on the immobilization of TiO$_2$ on suitable support materials to alleviate the recovery efficiency of TiO$_2$. Among the various support materials, activated carbon [14,15], glass [16], silica [17], graphene [18], and zeolite [19,20] have been used as immobilization substrates to try to improve their separation and recovery in water treatment. Zeolites are promising as a support for TiO$_2$ because they are abundant, readily available, and inexpensive [21]. In addition, they exhibit a high specific surface area, excellent adsorption, and catalysis capacity [21,22]. For these reasons, numerous studies have been conducted to explore the utilization of TiO$_2$/zeolite composites as photocatalytic materials, focusing on optimizing the degradation rate of pollutants in various environmental applications. [23,24].

The synthesis of zeolites involves the use of precursors such as sodium silicate and sodium aluminate together with structuring agents and alkali sources, which can be synthesized from various natural sources that are rich in silica and alumina, known as pozzolans. Examples of these sources include volcanic ash, volcanic tuff, pozzolanic clays, minerals such as diatomite and kaolinite, and rice husk ash. According to the Instituto Geológico Minero y Metalúrgico del Perú, the city of Arequipa is considered a volcanic area where there are different types of volcanic deposits called ignimbrites [25]. The method of extraction and carving of ignimbrite, which is also called "sillar", generates a large amount of residue, so the raw material is wasted, which contributes to the non-valuation of natural resources. Thus, ignimbrite waste is currently a byproduct that is undervalued and underutilized. Huanca et al. [26] synthesized zeolite from ignimbrite material from the Arequipa area, obtaining a zeolite with high cation exchange capacity and promising applications in the remediation and mitigation of heavy metal contamination in industrial effluents. In addition, a study investigated ignimbrite coated with SiO$_2$-TiO$_2$ for NO$_x$ degradation [9].

On the other hand, methyl orange (MO, C$_{14}$H$_{14}$N$_3$NaO$_3$S) is an organic chemical compound used as a dye in the textile industry. It can act as a contaminant in water when released. Methyl orange is challenging to biodegrade, and as a result, it may persist in water, potentially causing adverse effects on aquatic ecosystems and water quality. For this reason, removal methods, such as heterogeneous photocatalysis, are sought to effectively decompose it and reduce its environmental impact in water [27].

Accordingly, the present research aims to develop a TiO$_2$/zeolite photocatalytic material using the sol-gel method. Zeolite was synthesized from "sillar" gravel through the hydrothermal method, and it was intended for the zeolite to serve as a support to enhance the photocatalytic discoloration properties of TiO$_2$. The evaluation was conducted using methyl orange as a model of an organic contaminant. To assess the properties of TiO$_2$/zeolite and its precursors, X-ray diffraction (XRD), field-emission scanning electron microscopy (FE-SEM), reflectance (%R) (using a UV–visible spectrophotometer equipped with an integrating sphere), and Brunauer–Emmett–Teller (BET) surface area analyses were performed. Finally, dye decolorization under UV light irradiation was performed by comparing the photocatalytic performance of TiO$_2$/zeolite and pristine TiO$_2$ samples.

2. Materials and Methods

2.1. Materials

All chemicals utilized were of analytical grade and employed without additional purification. Hydrochloric acid (HCl, 37%), titanium (IV) Isopropoxide (C$_{12}$H$_{28}$O$_4$Ti, 97%), absolute ethyl alcohol (C$_2$H$_5$OH, 99.5%), and sodium hydroxide (NaOH, ≥99.9999%) were used for the synthesis of TiO$_2$ nanoparticles. Anatase-grade TiO$_2$ with 99.7% purity from Sigma Aldrich (Merck Peruana S.A., Lima, Perú) was acquired for comparison. Ignimbrite remainders were purchased from the Añashuayco quarries from Arequipa. Ultrapure and distilled water were used in all processes.

2.2. Obtaining Zeolite from Ignimbrite Residue

The natural ignimbrite remainders used in this study were obtained from Añashuayco quarry, Arequipa GD (latitude: −16.3592070, length: −71.6085700). The ignimbrite remainders were reduced to smaller parts as required. Then, through a milling process in a planetary ball mill (MP100-Retsch, Retsch, Düsseldorf, Germany) at 440 rpm for 30 min, the powder obtained was sieved to homogenize the granulometry with a 200 µm mesh size.

The synthesis of zeolite was realized through hydrothermal treatment using 120 mL of NaOH-3M with 15 g of milling ignimbrite residue. The mixture was placed in a stainless-steel autoclave and finally placed in a furnace at 180 °C for 24 h.

After this time, it was cooled at room temperature in the autoclave. The resulting solid was washed with distilled water until a pH of 7 was reached, and this was carried out in 10 replicates of 300 mL of distilled water through sonication and centrifugation. Finally, the resulting zeolite was dried in a furnace at 100 °C for 12 h.

2.3. Synthesis of TiO_2 Nanoparticles and the TiO_2/Zeolite Material

Titanium (IV) isopropoxide served as the titanium source when preparing the TiO_2/Zeolite photocatalyst. The titanium precursor solution was prepared by following the method by Hosseini et al. [28]. Initially, 10 mL of titanium (IV) isopropoxide was added dropwise to 30 mL of absolute ethyl alcohol and stirred for 60 min at room temperature. Subsequently, 1 g of synthesized zeolite was added, and the mixture was continuously stirred at 70 °C for 30 min.

After that, a hydrolysis catalyst solution was prepared by stirring 3 mL of HCl in 150 mL of ultrapure water for 10 min. This solution was then gradually added to the mixture of titanium (IV) isopropoxide, ethanol, and zeolite, with continuous stirring at 70 °C for 80 min. The mixture was dried at 100 °C for 16 h to evaporate the solvent. Finally, the resulting dry powders were calcined at 300 °C for 1 h to produce TiO_2/zeolite compounds, which primarily exhibited the anatase phase of TiO_2 [29].

On the other hand, to obtain pure TiO_2 for the tests, the same steps as those of the previously described sol-gel method were followed, excluding the addition of zeolite in the procedure.

2.4. Characterization

Various characterization tests were performed to compare the features among the zeolite, TiO_2, and TiO_2/zeolite samples. In the case of pure TiO_2, two types were used: those that were commercially obtained from Sigma-Aldrich and a sample synthesized according to what was described above. The crystal structure and identification of the phases in the obtained samples were analyzed using an X-ray diffractometer (XRD, Aeris Research, Malvern PANalytical, Malvern, UK) equipped with a CuKα radiation source (λ = 1.5406 Å). Morphological analyses were conducted through scanning electron microscopy (Scios 2, ThermoFisher Scientific, Waltham, MA, USA), and energy-dispersive X-ray spectroscopy (EDS, Thermo Scientific, UltraDry) was utilized for elemental chemical analysis with a working range of 20–25 keV.

To estimate the energy of the band gap of semiconductors, it is crucial to highlight the effectiveness of contemporary methodologies, such as the photoacoustic methodology, in meticulously deciphering the distinct contributions of scattering and absorption. These advanced techniques, which are grounded in the Kubelka–Munk theory, provide a sophisticated perspective on the intricacies of semiconductors, facilitating a more detailed exploration of their energy gap characteristics [30–32]. In this study, the optical properties of the samples were tested using a UV-vis DRS (diffuse reflectance spectroscopy) spectrophotometer (Perkin Elmer, Waltham, MA, USA) equipped with an integration sphere in the wavelength range of 200–700 nm. The energy band gaps (E_g) were determined

using the Kubelka–Munk theory and Tauc plot analysis, as per Equations (1) and (2), respectively [33].

$$F(R) = \left[\frac{K}{S}\right] \qquad (1)$$

$$[F(R_\infty) \, x \, h\nu]^{1/p} = A\left(h\nu - E_g\right) \qquad (2)$$

where K and S are the absorption and scattering coefficients, $h\nu$ is the photon energy, E_g is the optical band gap energy, and A is a proportionality constant independent of the photon energy [34]. To determine the band gap energy (E_g), a linear fit to a plot of $[F(R_\infty) x \, h\nu]^{1/p}$ versus $h\nu$ must be obtained through extrapolation to zero. In the case of an indirect band gap, such as that of TiO_2, a value of $p = 2$ will be used [33,34].

The textural properties of the samples were assessed through nitrogen isotherms at 77 K using a Micromeritics Gemini VII (Micromeritics, Norcross, GA, USA), where each sample (approximately 0.2 g) underwent a preliminary degassing at 200 °C for 2 h. The specific surface area was determined using the multipoint BET calculation method by following the BET expression in its linear form as outlined by Müller [35].

2.5. Photocatalytic Activity

The photocatalytic activity of the TiO_2/zeolite composite was evaluated by decolorizing aqueous solutions containing methyl orange (MO) at concentrations of 10 and 20 ppm. In each test, 0.6 g of the photocatalyst was dispersed in 200 mL of the corresponding MO solution. Subsequently, the suspension was illuminated with a 300 W OSRAM Ultravitalux lamp, where $70 \, Wm^{-2}$ was measured in the UV-A intensity range. The experiments were realized at room temperature. During irradiation, 10 mL of the treated solution was collected every 10 min and centrifuged at 6000 rpm for 4 min. Then, the supernatant was removed, and another centrifugation was performed at 6000 rpm for 2 min, resulting in a clear solution. The remaining concentration of methyl orange was analyzed using a Lambda 365 UV-vis spectrophotometer (PerkinElmer, Waltham, MA, USA) at 507 nm. A comparison of the photocatalytic efficiency of the TiO_2/zeolite composite and pure TiO_2 was carried out. The methyl orange removal efficiency in percentage degradation ($\%Eff_{deg}$) was calculated with Equation (3) [27]:

$$\%Eff_{deg} = \left[\frac{C_0 - C_t}{C_0}\right] \times 100\% \qquad (3)$$

where C_0 and C_t represent the initial concentration of the MO solution and the concentration of MO analyzed after light irradiation during a specific time interval, respectively.

3. Results and Discussion

3.1. XRD Analysis

Figure 1 shows the XRD patterns of the ignimbrite precursor material, zeolite, TiO_2/zeolite, and pure TiO_2 obtained with the sol-gel method. The ignimbrite pattern reveals that its main identified crystalline phase is anorthoclase, followed by cristobalite and albite. Anorthoclase is a feldspar composed of aluminum silicates with varying percentages of potassium, sodium, and calcium [36,37]. Furthermore, the obtained peaks are primarily located between angles of 15° and 40° (2θ), which is consistent with zeolite synthesis studies by Rajakrishnamoorthy et al. [38] and Verrecchia et al. [39]. The open halo that was observed suggests thermodynamically metastable amorphous aluminosilicate structures with high pozzolanic activity [40].
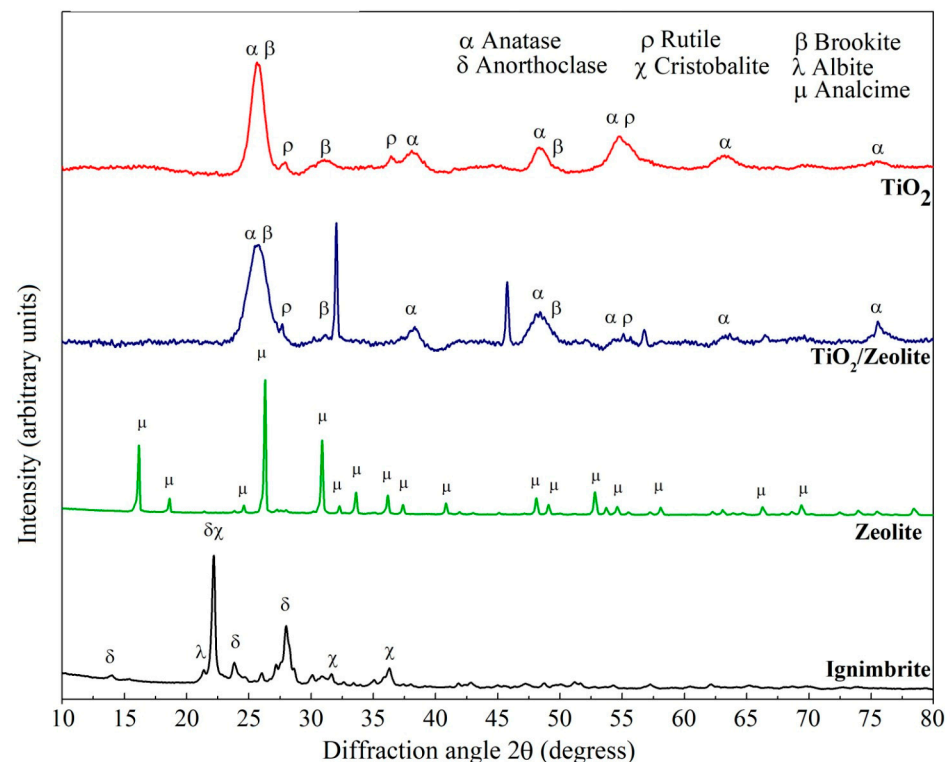
Figure 1. X-ray diffraction patterns for TiO$_2$, TiO$_2$/zeolite, zeolite, and ignimbrite samples.

The zeolite pattern shows that the peaks of ignimbrite decreased, whereas new peaks appeared. This reduction in initial crystalline phases may be attributed to the dissolution of precursors with an alkaline solution, contributing to the increase in silicate and aluminate solutions present in these [41]. This assumption is supported by the study by Ojha et al. [42], where a reduction in the intensity of quartz and mullite was observed after the synthesis process using NaOH. The zeolite spectrum indicated characteristic peaks at 2θ = 15.7°, 18.1°, 25.8°, and 30.4° corresponding to the analcime-type zeolite structure (JCPDS no. 76-0904) [43].

Finally, the XRD patterns of the TiO$_2$ and TiO$_2$/zeolite catalysts evidence characteristic peaks for the anatase phase (JCPDS no. 96-901-5930) that were observed at approximately 25.3°, 37.7°, 48.0° 54.1°, and 62.6° [44]; a rutile phase (JCPDS no. 01-078-1510) was detected in a small proportion [45]. No significant changes were observed in the TiO$_2$ peaks after incorporating zeolite. However, in the TiO$_2$/zeolite compound, two additional peaks corresponding to analcime zeolite were observed. Therefore, the TiO$_2$/zeolite photocatalytic material exhibits the structure of the TiO$_2$ component in the anatase phase along with peaks corresponding to the analytical structure of zeolite.
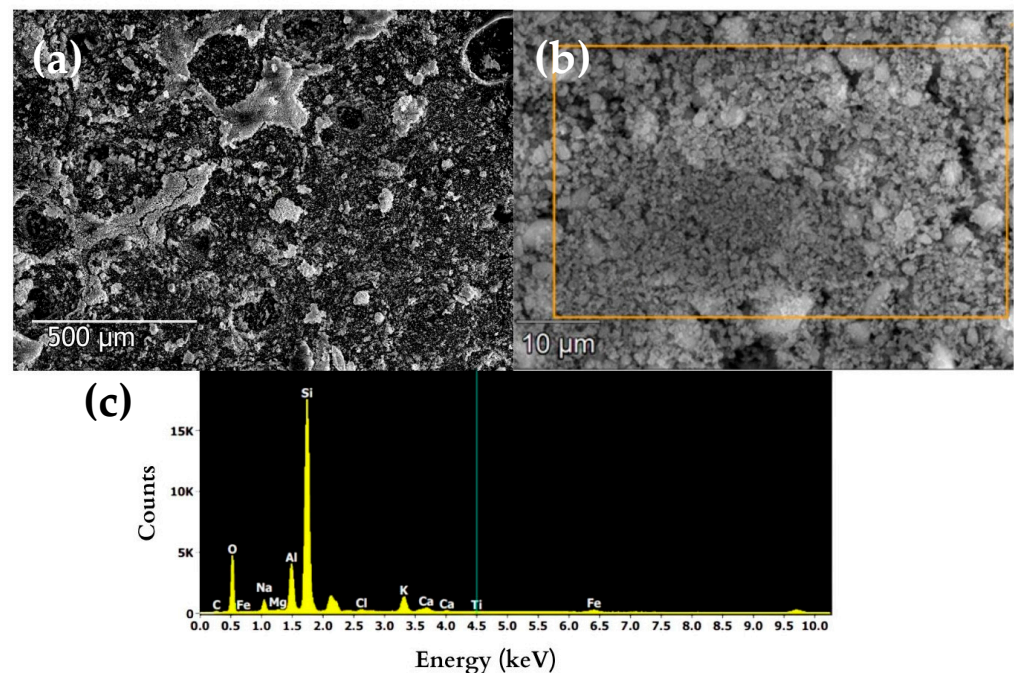
3.2. SEM Analysis

The samples were analyzed using scanning electron microscopy to examine their surface morphology, interactions, particle size, and elemental chemical composition. The weight percentages of the significant oxides are shown in Table 1, and silicon dioxide (SiO$_2$) was the predominant component in the ignimbrite, zeolite, and TiO$_2$/zeolite samples. The term "others" in Table 1 includes MgO, K$_2$O, CaO, and Fe$_2$O$_3$ oxides.

Table 1. Weight percentages of oxides in the samples.

| Oxides | Weight Percentage % | | | |
	Ignimbrite	Zeolite	TiO$_2$	TiO$_2$/Zeolite
SiO$_2$	74.97	54.72	----	73.55
Al$_2$O$_3$	13.52	19.60	----	5.77
Na$_2$O	4.38	12.98	----	1.06
TiO$_2$	0.18	0.52	99.52	17.54
Cl	0.37	0.83	0.48	1.18
Others	6.58	11.35	----	0.90
Total	100	100	100	100

3.2.1. Ignimbrite

SEM micrographs of the precursor material (ignimbrite), which was previously milled and passed through a 200 μm mesh, are shown in Figure 2a. The figure reveals agglomerated particles with a varied morphology, suggesting a particle size below 100 μm, which was consistent with the expected milling size. The EDS chemical composition analysis is shown in Figure 2c. In this sample, large amounts of silicon, aluminum, and oxygen were revealed, demonstrating the siliceous nature of ignimbrite, which favors zeolite synthesis. The spectrum also shows signals related to CaO and Fe$_2$O$_3$, which could negatively affect the synthesis process [46].

Figure 2. SEM micrograph of (**a**) milling ignimbrite and (**b**) the analyzed area of ignimbrite. (**c**) EDS of the area analyzed in (**b**).

3.2.2. Zeolite

SEM micrographs of the synthesized zeolite are shown in Figure 3a,b. The measured size of the synthesized zeolites ranges from 9 μm to 46 μm, with an average dimension of approximately 45 μm. This average size notably exceeds the measurements reported by earlier researchers [47,48]. Furthermore, the particles exhibit an octahedral three-dimensional crystalline structure, a characteristic of analcime-type zeolite [49]. The EDS spectrum in Figure 3c and the oxide weight percentages listed in Table 1 for the obtained zeolite reveal that SiO$_2$ is the predominant component (54.72%), which is consistent with the starting material, whereas the oxides MgO, K$_2$O, CaO, and Fe$_2$O$_3$ comprise 11.35%.
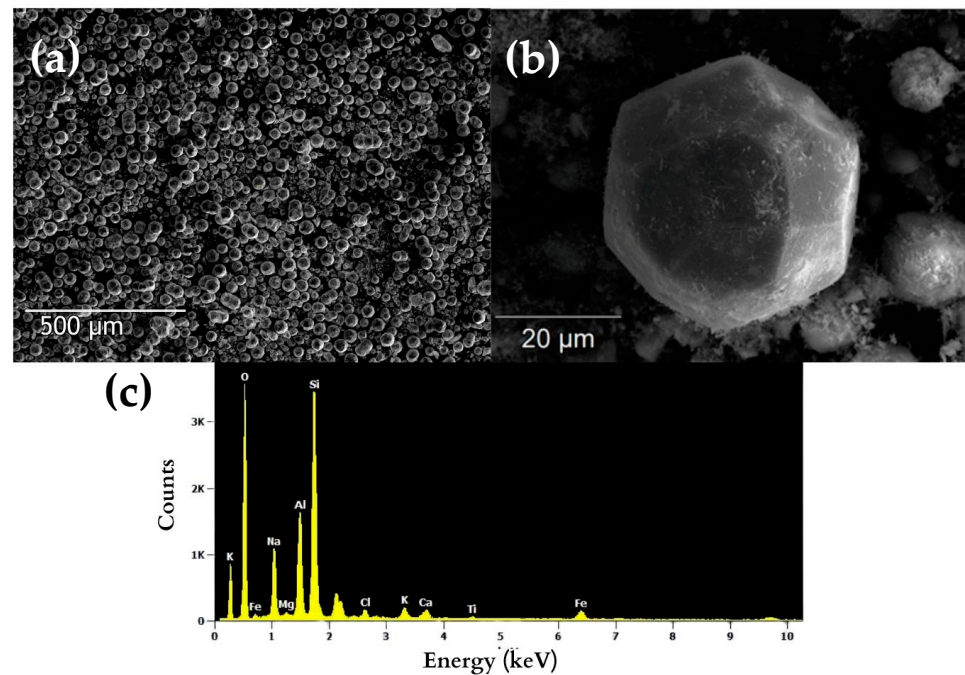
Figure 3. SEM micrographs of the synthesized zeolites at (**a**) low and (**b**) high magnification. (**c**) EDS of the whole area of the synthesized zeolite.

3.2.3. Synthesized TiO_2 Nanoparticles

SEM micrographs of the TiO_2 synthesized with the sol-gel method are presented in Figure 4a,b. These images reveal agglomerated TiO_2 nanoparticles, which, according to the measurements, exhibit a size range from 18 nm to 45 nm. In addition, it should be noted that in Figure 4c and Table 1, titanium oxide is the predominant component (99.52%).
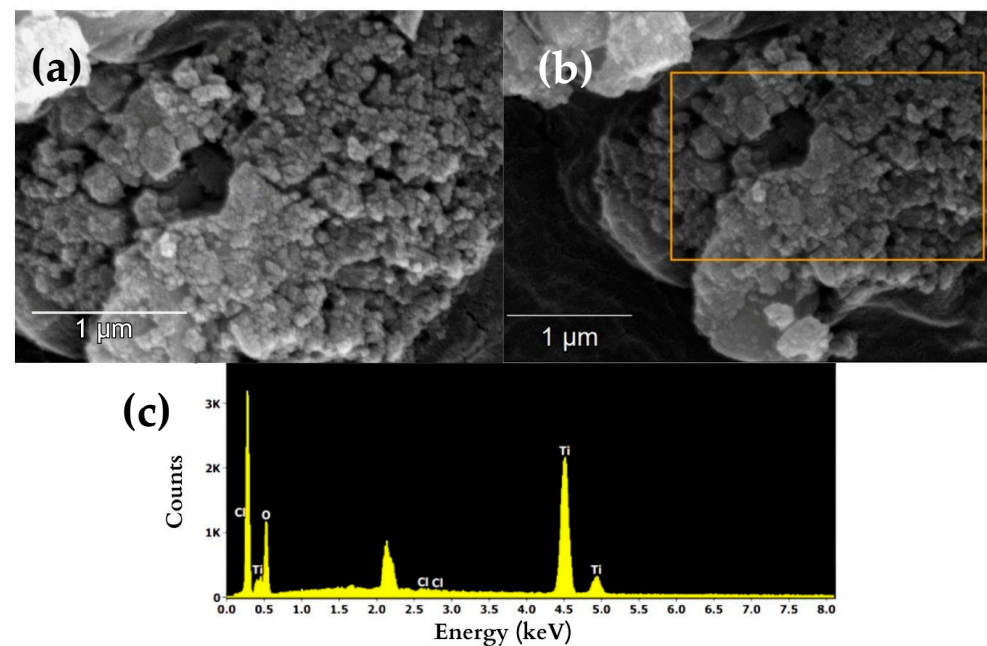

Figure 4. SEM micrograph of (**a**) the synthesized TiO_2 nanoparticles and (**b**) the analyzed nanoparticle area. (**c**) EDS of the entire area analyzed in (**b**).

3.2.4. TiO$_2$/Zeolite Photocatalytic Material

The SEM micrographs in Figure 5a,b exhibit the morphology of the TiO$_2$/zeolite photocatalyst synthesized via the sol-gel method. The images confirm the presence of zeolite and TiO$_2$ nanoparticles, aligning with the EDS analysis and consistent with findings from prior studies [13,50,51]. The diameter of the TiO$_2$ nanoparticles on the zeolite surface was determined to be in the range from 15 nm to 47 nm. Furthermore, the TiO$_2$/zeolite composite demonstrates enhanced material dispersion within its structure compared to that in the pure TiO$_2$ sample. The EDS spectrum (Figure 5c) and Table 1 reveal that SiO$_2$ and TiO$_2$ are the predominant components, constituting the majority, while the remaining 0.90% comprises various other oxides.
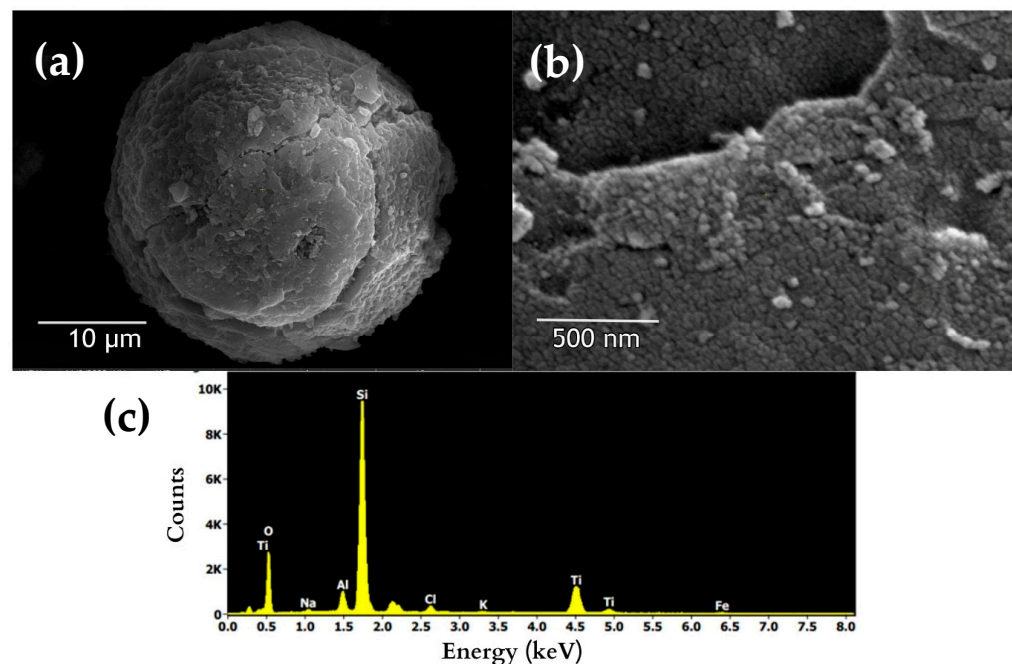

Figure 5. SEM micrograph of (**a**) the TiO$_2$/zeolite photocatalytic material and (**b**) the analyzed nanoparticle area. (**c**) EDS of the entire area analyzed in (**b**).

3.3. UV–Visible Spectroscopy

The determination of the band gap is a crucial characterization for photocatalytic materials, as it plays a significant role in the photocatalytic reaction—specifically, in light absorption and the generation of electron–hole pairs [52]. According to the Kubelka–Munk model and the extrapolation of the linear adjustment to zero, the corresponding Tauc plot was created for commercial pure TiO$_2$ (Figure 6a), synthesized TiO$_2$ (Figure 6b), and TiO$_2$/zeolite (Figure 6c) with Equations (1) and (2). The results, which are summarized in Table 2, reveal that the calculated band gap for TiO$_2$/zeolite is 3.14 eV, which is smaller than the values obtained for commercial TiO$_2$ (3.29 eV) and synthesized TiO$_2$ (3.18 eV) and is in proximity to the reported values [53–55]. These values imply activation only with a UV light source [56]. In addition, the band gap of TiO$_2$/zeolite implies heightened light absorption, which leads to an increased generation of excited charge carriers and, consequently, enhances photocatalytic activity.
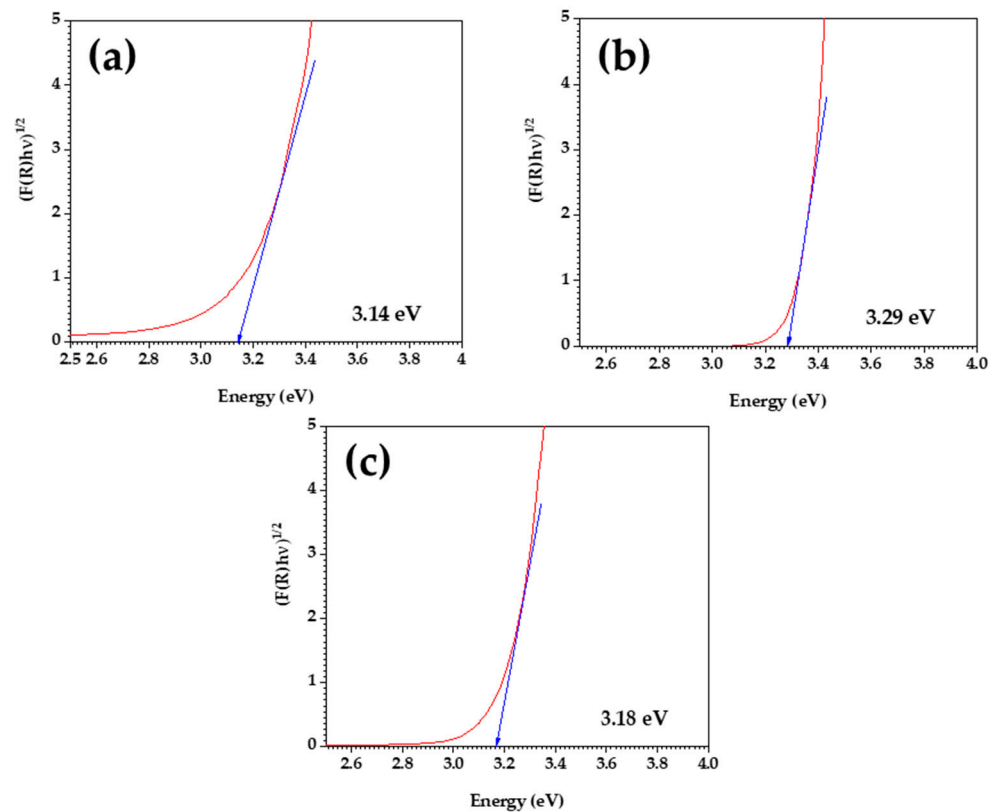
Figure 6. Indirect band gaps calculated for (**a**) TiO_2 from Sigma Aldrich, (**b**) synthesized TiO_2, and (**c**) TiO_2/zeolite. The red line represents the Tauc plot image, and the tangent blue line indicates the estimated band gap energy from the linear fit.

Table 2. The calculated band gaps of the samples.

Sample	Band Gap (eV)
TiO_2/zeolite	3.14
TiO_2—Sigma Aldrich	3.29
Synthesized TiO_2	3.18

3.4. Physisorption Test Parameters

The BET surface area, pore volume, mean pore diameter, and particle size constitute interconnected characteristics that are essential for optimizing the photocatalytic efficiency of a material [57]. In this case study, these parameters were assessed through physisorption testing, and the findings are detailed in Table 3. The results indicated that the TiO_2/zeolite material exhibited the highest surface area (169.079 $\pm$ 0.802 m^2/g), surpassing those of the synthesized TiO_2 (86.951 $\pm$ 0.346 m^2/g), the commercial TiO_2 from Sigma Aldrich (80.571 $\pm$ 0.278 m^2/g), and zeolite analcime (1.740 $\pm$ 0.005 m^2/g). The zeolite analcime exhibited the lowest surface area value, which was characteristic of this structure type due to its high-temperature synthesis [49]. On the other hand, the value obtained for TiO_2/zeolite was approximately double that of the synthesized pure TiO_2. The high surface area and porous structure obtained for this material favor the adsorption, desorption, and diffusion of reagents, resulting in high photocatalytic activity [58]. Furthermore, the other measured parameters, such as the pore volume and pore size, in the TiO_2/zeolite composite also exhibit the highest values compared to those of the other samples, as indicated in Table 3.

Table 3. The textural properties of all samples.

Sample	Surface Area [m^2/g]	Pore Volume [cm^3/g]	Average Pore Diameter [nm]
Zeolite analcime	1.740 ± 0.005	0.000489	2.1426
TiO$_2$—Sigma Aldrich	80.571 ± 0.278	0.022379	2.1420
Synthesized TiO$_2$	86.951 ± 0.346	0.025958	2.1505
TiO$_2$/zeolite	169.079 ± 0.802	0.042061	2.1411

3.5. Photocatalytic Performance Results

To evaluate the photocatalytic activity, the photodegradation of methyl orange dye was measured at concentrations of 10 and 20 ppm in aqueous solutions under UV light. The photocatalytic activity results for 10 and 20 ppm are shown in Figure 7, with C_t/C_o representing the ratio of the concentration at time "t" to the initial concentration of methyl orange over time in minutes. The highest photocatalytic efficiency during the first 60 min under UV light irradiation was observed for the TiO$_2$/zeolite sample compared to pure TiO$_2$ in the anatase phase for both concentrations. The percentage of degradation efficiency was calculated according to Equation (3), and the results are shown in Table 4. For a concentration of 10 ppm, the TiO$_2$/zeolite synthesized from ignimbrite residue as a source of zeolite degraded 94.71% of the dye in the first 60 min, while the synthesized TiO$_2$ degraded 83.93%, which was 10.78% lower. For the case of 20 ppm, the TiO$_2$/zeolite photocatalyst (71.36%) also demonstrated higher efficiency than that of pure TiO$_2$ (56.78%). The pH remained constant at 3.5 for all cases.

Table 4. Comparison of the degradation efficiency for the samples.

Sample	Concentration [ppm]	%Eff_{deg}
TiO$_2$/zeolite	10	94.71
Pure synthesized TiO$_2$	10	83.93
TiO$_2$/zeolite	20	71.36
Pure synthesized TiO$_2$	20	56.78

The photodegradation of MO with the various photocatalysts was fitted to the pseudo-first-order kinetic model [59]:

$$\ln\left(\frac{C_o}{C_t}\right) = kt \tag{4}$$

where C_t, C_0, and k represent the residual MO concentration, initial MO concentration, and pseudo-first-order rate constant, respectively. Figure 8 displays a graph representing the relationship between $\ln(C_0/C_t)$ and time for various concentrations of MO when utili-zing TiO$_2$/zeolite and pristine TiO$_2$ as photocatalysts. A robust fit for the first-order model was achieved, with a correlation coefficient (R^2) exceeding 0.90 in all cases, as depicted in Table 5. Additionally, the rate constant was determined from these graphs, and the results are presented in Table 5. As shown in the figure and table, TiO$_2$/zeolite exhibited the highest rate constants for the photodegradation of MO both for the concentration of 10 ppm (0.0436 min^{-1}) and for that of 20 ppm (0.0207 min^{-1}), and they were higher than those obtained for pure TiO$_2$ (0.0286 min^{-1} and 0.0139 min^{-1} for 10 and 20 ppm, respectively). The enhanced efficiency of the TiO$_2$/zeolite photocatalytic material was attributed to the presence of zeolite, which facilitated the adsorption of the dye and the interaction with TiO$_2$ to break down these organic dyes, which agreed with other studies that were carried out [13,15,21]. The synergy of TiO$_2$ nanoparticles with zeolite boosts the photocatalytic activity by leveraging zeolites' high surface area and many active sites for enhanced adsorption of methyl orange [13]. This combination prevents nanoparticle aggregation and amplifies light adsorption. Furthermore, zeolites act as electron sinks, diminishing

electron–hole recombination and prolonging electron lifetime [13,21]. Consequently, this enhances the overall photocatalytic activity of the material.
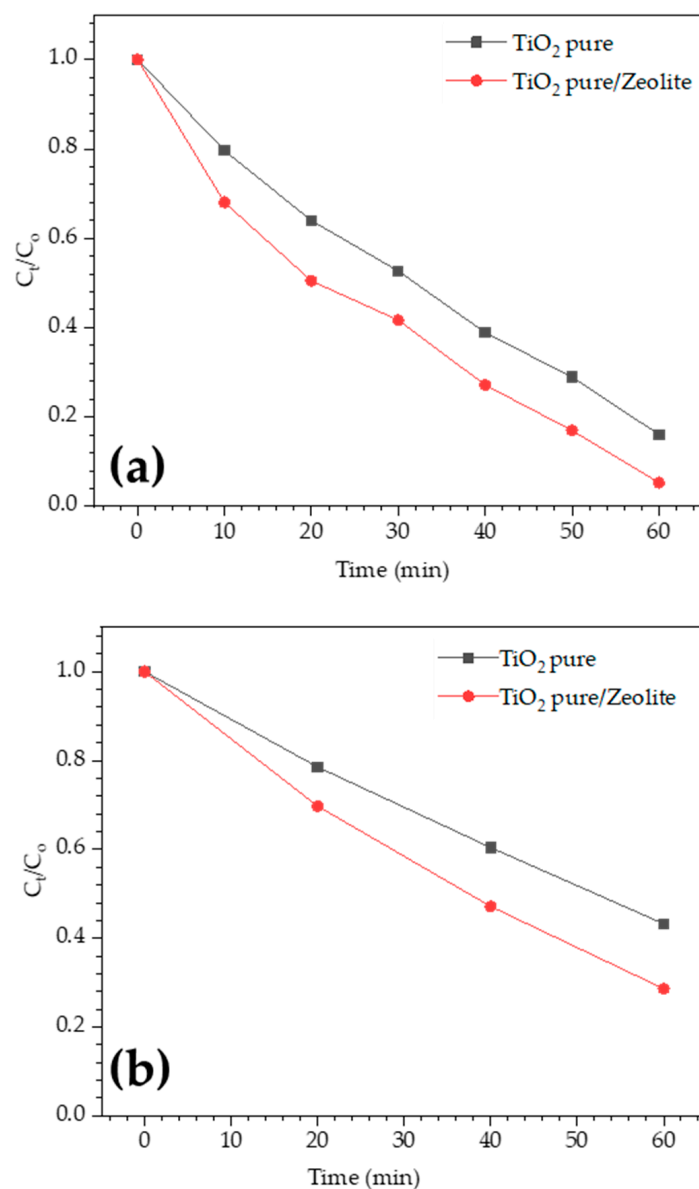

Figure 7. Photodegradation of methyl orange using pure TiO_2 and TiO_2/zeolite material at concentrations of (**a**) 10 ppm and (**b**) 20 ppm.

Table 5. Kinetic parameters in the photocatalytic experiments.

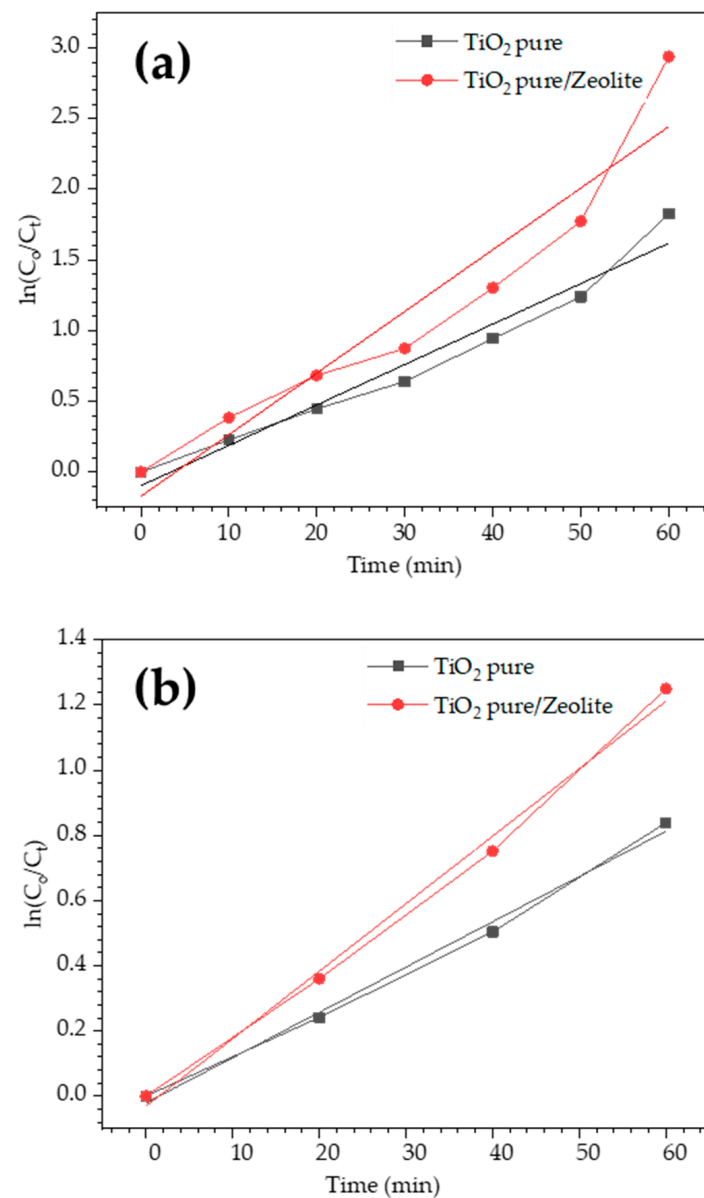| Sample	Concentration [ppm]	k (min^{-1})	R^2
TiO_2/zeolite	10	0.0436	0.963
Pure synthesized TiO_2	10	0.0286	0.917
TiO_2/zeolite	20	0.0207	0.994
Pure synthesized TiO_2	20	0.0139	0.994

Figure 8. $\ln(C_0/C_t)$ as a function of time for the photodegradation of methyl orange at concentrations of (**a**) 10 ppm and (**b**) 20 ppm for TiO_2/zeolite and pure TiO_2.

3.5.1. Effect of Catalyst Loading

In photocatalysis, the degradation efficiency is affected by the photocatalyst dose. To examine the effect of the catalyst dose on the photodegradation of MO for 30 min, the amount of TiO_2/zeolite was varied from 0.2 to 1 g at a constant MO concentration of 10 ppm. As shown in Figure 9, as the amount of photocatalyst increased from 0.2 to 1 g, the MO degradation efficiency increased (0%, 45%, 58%, 88%, and 95% for 0.2, 0.4, 0.6, 0.8, and 1 g, respectively). This occurs because a higher catalyst concentration offers additional active sites for redox reactions. In other words, irradiation produces more charge carriers to participate in redox reactions [60].
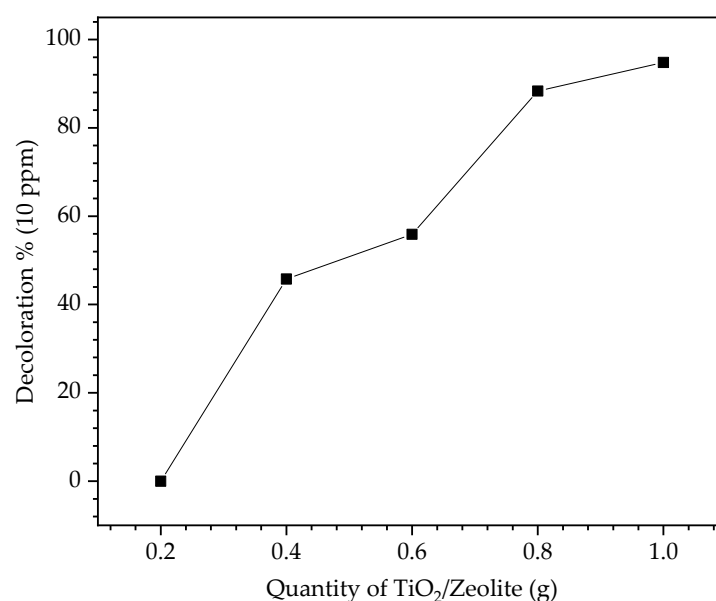
Figure 9. Photodegradation efficiency of MO using various amounts of TiO$_2$/zeolite for 30 min.

3.5.2. The Reusability Study

The study of photocatalytic applications places significant importance on reusability. This aspect is crucial, as it enables us to determine whether a photocatalyst can be effectively reused in wastewater treatment. Given this, to evaluate the reusability of the TiO$_2$/zeolite composite, three consecutive tests of degradation of MO were conducted under the same reaction conditions. As shown in Table 6, the TiO$_2$/zeolite photocatalysts retain their ability to degrade MO solutions at 10 ppm even after three uses, showing a slight difference from the initial experiment. However, for 20 ppm solutions of MO, the sample presents a considerable decrease in its degradation efficiency after two cycles. The loss might be attributed to the catalyst leaching that inevitably occurs during the recovery and washing process, as well as the blocking of the active site by the surface coverage with the dye and its degradation intermediates [61].

Table 6. Reutilization of TiO$_2$/zeolite for the photodegradation of methyl orange.

Sample	Degradation Efficiency (%)	Concentration
TiO$_2$/zeolite (First Test)	92.80	
TiO$_2$/zeolite (Second Test)	88.15	10 ppm
TiO$_2$/zeolite (Third Test)	87.64	
TiO$_2$/zeolite (First Test)	70.20	
TiO$_2$/zeolite (Second Test)	67.69	20 ppm
TiO$_2$/zeolite (Third Test)	18.06	

3.5.3. Comparative Analysis

The TiO$_2$/zeolite photocatalyst was compared with previously reported photocatalysts for the photodegradation of organic dyes, and the results are noted in Table 7. It should be noted that while the presented photocatalyst is comparable and even improved with respect to those reported in the literature, direct comparisons are challenging due to differences in dye type and its initial concentration, light source, catalyst morphology, irradiation time, and source of zeolite. In this research, the source of zeolite was ignimbrite, which is a good source of zeolites used in the synthesis of photocatalytic materials. Therefore, these considerations suggest that the TiO$_2$/zeolite presented here is a novel and suitable material for the photodegradation of methyl orange.

Table 7. Comparison of the photocatalytic performance for different TiO_2/zeolite materials.

Sample	Degradation/Time Test	Concentration
TiO_2/zeolite (this work)	94.71%/60 min	10 ppm
TiO_2/zeolite [23]	77.68%/60 min	10 ppm
TiO_2/SDS [50]	90%/300 min	30 ppm
TiO_2 layers on glass substrates—3 layers [16]	97.6%/180 min	30 ppm
TiO_2/zeolite (this work)	71.36%/60 min	20 ppm
TiO_2/zeolite [23]	68.61%/60 min	20 ppm

4. Conclusions

In summary, a TiO_2/zeolite photocatalytic material was synthesized through the sol-gel method to facilitate the degradation of organic dyes. The zeolite, which was sourced from ignimbrite residues from the Añashuayco quarry in Arequipa, was obtained in its analcime type, while the TiO_2 was obtained in its anatase form, which is preferred for its photocatalytic activity. Furthermore, the synthesized pure TiO_2 showed a band gap and physisorption parameters like those of commercial TiO_2. Meanwhile, the TiO_2/zeolite photocatalytic material exhibited superior physisorption properties and dye degradation, achieving a photocatalytic efficiency of 94.71% and 83.93% for solutions of 10 and 20 ppm, respectively, in 60 min. This occurred due to its high specific surface area ($169.0788 \ m^2/g$), larger pore volume ($0.04 \ cm^3/g$), and band gap of 3.14 eV. On the other hand, the TiO_2/zeolite photocatalytic material can be reused in photocatalytic applications with slight changes in its performance. However, at higher concentrations, this reusability decreases. Zeolite improved the photodegradation performance of the TiO_2/zeolite material due to its influence on the surface morphology and interaction, favoring the uniform dispersion of TiO_2 nanoparticles and providing more active sites for the adsorption of contaminants. Thus, this TiO_2/zeolite photocatalytic material based on zeolite obtained from ignimbrite residue effectively removes organic dyes such as methyl orange from water, demonstrating high efficiency and potential applications in wastewater treatment.

Institutional Review Board Statement: Not applicable.

Informed Consent Statement: Not applicable.

Data Availability Statement: The data presented in this study are available on request from the corresponding author. The data are not publicly available due to privacy.

Conflicts of Interest: The authors declare no conflicts of interest. The funders had no role in the design of the study, in the collection, analyses, or interpretation of data, in the writing of the manuscript, or in the decision to publish the results.

References

1. Crini, G.; Lichtfouse, E. Wastewater Treatment: An Overview. In *Green Adsorbents for Pollutant Removal*; Springer: Berlin, Germany, 2018; pp. 1–21. [CrossRef]

2. Abdellah, M.H.; Nosier, S.A.; El-Shazly, A.H.; Mubarak, A.A. Photocatalytic Decolorization of Methylene Blue Using TiO$_2$/UV System Enhanced by Air Sparging. *Alex. Eng. J.* **2018**, *57*, 3727–3735. [CrossRef]

3. Khataee, A.R.; Pons, M.N.; Zahraa, O. Photocatalytic Degradation of Three Azo Dyes Using Immobilized TiO$_2$ Nanoparticles on Glass Plates Activated by UV Light Irradiation: Influence of Dye Molecular Structure. *J. Hazard. Mater.* **2009**, *168*, 451–457. [CrossRef] [PubMed]

4. Peng, H.; Guo, J. Removal of chromium from wastewater by membrane filtration, chemical precipitation, ion exchange, adsorption electrocoagulation, electrochemical reduction, electrodialysis, electrodeionization, photocatalysis and nanotechnology: A review. *Environ. Chem. Lett.* **2020**, *18*, 2055–2068. [CrossRef]

5. Ahmad, A.; Mohd-Setapar, S.H.; Chuong, C.S.; Khatoon, A.; Wani, W.A.; Kumar, R.; Rafatullah, M. Recent advances in new generation dye removal technologies: Novel search for approaches to reprocess wastewater. *RSC Adv.* **2015**, *5*, 30801–30818. [CrossRef]

6. Ameta, R.; Solanki, M.S.; Benjamin, S.; Ameta, S.C. Photocatalysis. In *Advanced Oxidation Processes for Wastewater Treatment: Emerging Green Chemical Technology*; Elsevier Inc.: Amsterdam, The Netherlands, 2018; pp. 135–175. [CrossRef]

7. Ramos, P.G.; Espinoza, J.; Sánchez, L.A.; Rodriguez, J.M. Enhanced photocatalytic degradation of Rhodamine B employing transition metal (Fe, Cu, Co) doped ZnO/rGO nanostructures synthesized by electrospinning-hydrothermal technique. *J. Alloys Compd.* **2023**, *966*, 171559. [CrossRef]

8. Ângelo, J.; Magalhães, P.; Andrade, L.; Mendes, A. Characterization of TiO$_2$-based semiconductors for photocatalysis by electrochemical impedance spectroscopy. *Appl. Surf. Sci.* **2016**, *387*, 183–189. [CrossRef]

9. Florez, D.M.M.G.; Ale, R.B.G.; Idme, A.F.H.; Alarcon, L.A.L.; Huallpa, E.A.; Castro, Y.; Apestegui, P.G.R.; Rodriguez, J.M.R. SiO$_2$-TiO$_2$ Films Supported on Ignimbrite by Spray Coating for the Photocatalytic Degradation of NO$_x$ Gas and Methyl Orange Dye. *Int. J. Photoenergy* **2020**, *2020*, 4756952. [CrossRef]

10. Nakata, K.; Fujishima, A. TiO$_2$ Photocatalysis: Design and Applications. *J. Photochem. Photobiol. C Photochem. Rev.* **2012**, *13*, 169–189. [CrossRef]

11. Guo, Q.; Zhou, C.; Ma, Z.; Yang, X. Fundamentals of TiO$_2$ Photocatalysis: Concepts, Mechanisms, and Challenges. *Adv. Mater.* **2019**, *31*, 1901997. [CrossRef]

12. Sarkar, A.K.; Saha, A.; Tarafder, A.; Panda, A.B.; Pal, S. Efficient Removal of Toxic Dyes via Simultaneous Adsorption and Solar Light Driven Photodegradation Using Recyclable Functionalized Amylopectin-TiO$_2$-Au Nanocomposite. *ACS Sustain. Chem. Eng.* **2016**, *4*, 1679–1688. [CrossRef]

13. Zhang, G.; Song, A.; Duan, Y.; Zheng, S. Enhanced Photocatalytic Activity of TiO$_2$/Zeolite Composite for Abatement of Pollutants. *Microporous Mesoporous Mater.* **2018**, *255*, 61–68. [CrossRef]

14. Fu, X.; Yang, H.; Lu, G.; Tu, Y.; Wu, J. Improved performance of surface functionalized TiO$_2$/activated carbon for adsorption–photocatalytic reduction of Cr(VI) in aqueous solution. *Mater. Sci. Semicond. Process* **2015**, *39*, 362–370. [CrossRef]

15. Martins, A.C.; Cazetta, A.L.; Pezoti, O.; Souza, J.R.B.; Zhang, T.; Pilau, E.J.; Asefa, T.; Almeida, V.C. Sol-gel synthesis of new TiO$_2$/activated carbon photocatalyst and its application for degradation of tetracycline. *Ceram. Int.* **2017**, *43*, 4411–4418. [CrossRef]

16. Bouarioua, A.; Zerdaoui, M. Photocatalytic activities of TiO$_2$ layers immobilized on glass substrates by dip-coating technique toward the decolorization of methyl orange as a model organic pollutant. *J. Environ. Chem. Eng.* **2017**, *5*, 1565–1574. [CrossRef]

17. Kuo, H.P.; Yao, S.W.; Huang, A.N.; Hsu, W.Y. Photocatalytic degradation of toluene in a staged fluidized bed reactor using TiO$_2$/silica gel. *Korean J. Chem. Eng.* **2017**, *34*, 73–80. [CrossRef]

18. Kusiak-Nejman, E.; Morawski, A.W. TiO$_2$/graphene-based nanocomposites for water treatment: A brief overview of charge carrier transfer, antimicrobial and photocatalytic performance. *Appl. Catal. B* **2019**, *253*, 179–186. [CrossRef]

19. Liu, X.; Liu, Y.; Lu, S.; Guo, W.; Xi, B. Performance and mechanism into TiO$_2$/Zeolite composites for sulfadiazine adsorption and photodegradation. *Chem. Eng. J.* **2018**, *350*, 131–147. [CrossRef]

20. Badvi, K.; Javanbakht, V. Enhanced photocatalytic degradation of dye contaminants with TiO$_2$ immobilized on ZSM-5 zeolite modified with nickel nanoparticles. *J. Clean. Prod.* **2021**, *280*, 124518. [CrossRef]

21. Setthaya, N.; Chindaprasirt, P.; Yin, S.; Pimraksa, K. TiO$_2$-zeolite photocatalysts made of metakaolin and rice husk ash for removal of methylene blue dye. *Powder Technol.* **2017**, *313*, 417–426. [CrossRef]

22. Chong, M.N.; Tneu, Z.Y.; Poh, P.E.; Jin, B.; Aryal, R. Synthesis, characterisation and application of TiO$_2$–zeolite nanocomposites for the advanced treatment of industrial dye wastewater. *J. Taiwan. Inst. Chem. Eng.* **2015**, *50*, 288–296. [CrossRef]

23. Aziztyana, A.P.; Wardhani, S.; Prananto, Y.P.; Purwonugroho, D.; Darjito. Optimisation of Methyl Orange Photodegradation Using TiO$_2$-Zeolite Photocatalyst and H$_2$O$_2$ in Acid Condition. *IOP Conf. Ser. Mater. Sci. Eng.* **2019**, *546*, 042047. [CrossRef]

24. Rahman, A.; Nurjayadi, M.; Wartilah, R.; Kusrini, E.; Prasetyanto, E.A.; Degermenci, V. Enhanced Activity of TiO$_2$/Natural Zeolite Composite for Degradation of Methyl Orange under Visible Light Irradiation. *Int. J. Technol.* **2018**, *9*, 1159–1167. [CrossRef]

25. Lebti, P.P.; Thouret, J.C.; Wörner, G.; Fornari, M. Neogene and Quaternary ignimbrites in the area of Arequipa, Southern Peru: Stratigraphical and petrological correlations. *J. Volcanol. Geotherm. Res.* **2006**, *154*, 251–275. [CrossRef]

26. Huanca, P.K.; Corrales, L.T.; Paredes, B.; Almirón, J.J.; Gonzales, D.P. Estudio de la modificación hidrotermal de un mineral Ignimbrítico para obtener zeolita sintética de alta capacidad de intercambio catiónico. *Rev. Bol. Quim* **2019**, *36*, 173–180. [CrossRef]

27. Waghchaure, R.H.; Adole, V.A.; Jagdale, B.S. Photocatalytic degradation of methylene blue, rhodamine B, methyl orange and Eriochrome black T dyes by modified ZnO nanocatalysts: A concise review. *Inorg. Chem. Commun.* **2022**, *143*, 109764. [CrossRef]

28. Hosseini, M.S.; Sadeghi, M.T.; Khazaei, M. Wettability alteration from superhydrophobic to superhydrophilic via synthesized stable nano-coating. *Surf. Coat. Technol.* **2017**, *326*, 79–86. [CrossRef]

29. Mosquera, E.; Rosas, N.; Debut, A.; Guerrero, V.H. Síntesis y caracterización de nanopartículas de dióxido de titanio obtenidas por el método de sol-gel. *Rev. Politécnica* **2015**, *36*, 7.

30. Lamastra, F.R.; Grilli, M.L.; Leahu, G.; Belardini, A.; Li Voti, R.; Sibilia, C.; Salvatori, D.; Cacciotti, I.; Nanni, F. Photoacoustic Spectroscopy Investigation of Zinc Oxide/Diatom Frustules Hybrid Powders. *Int. J. Thermophys.* **2018**, *39*, 110. [CrossRef]

31. Lamastra, F.R.; Grilli, M.L.; Leahu, G.; Belardini, A.; Li Voti, R.; Sibilia, C.; Salvatori, D.; Cacciotti, I.; Nanni, F. Diatom frustules decorated with zinc oxide nanoparticles for enhanced optical properties. *Nanotechnology* **2017**, *28*, 375704. [CrossRef]

32. Li Voti, R.; Leahu, G.; Sibilia, C.; Matassa, R.; Familiari, G.; Cerra, S.; Salamone, T.A.; Fratoddi, I. Photoacoustics for listening to metal nanoparticle super-aggregates. *Nanoscale Adv.* **2021**, *3*, 4692–4701. [CrossRef]

33. Landi, S.; Segundo, I.R.; Freitas, E.; Vasilevskiy, M.; Carneiro, J.; Tavares, C.J. Use and misuse of the Kubelka-Munk function to obtain the band gap energy from diffuse reflectance measurements. *Solid. State Commun.* **2022**, *341*, 114573. [CrossRef]

34. López, R.; Gómez, R. Band-gap energy estimation from diffuse reflectance measurements on sol–gel and commercial TiO_2: A comparative study. *J. Sol-Gel Sci. Technol.* **2012**, *61*, 1–7. [CrossRef]

35. Müller, B.R. Preparation and characterization of K_2CO_3-doped powdered activated carbon for effective in-vitro adsorption of deoxynivalenol. *Bioresour. Technol.* **2021**, *15*, 100703. [CrossRef]

36. Klima, K.M.; Schollbach, K.; Brouwers, H.J.H.; Yu, Q. Enhancing the thermal performance of Class F fly ash-based geopolymer by sodalite. *Constr. Build. Mater.* **2022**, *314*, 125574. [CrossRef]

37. Cruz Sánchez, E.; Torres, M.E.; Diaz, C.; Saito, F. Effects of grinding of the feldspar in the sintering using a planetary ball mill. *J. Mater. Process. Technol.* **2004**, *152*, 284–290. [CrossRef]

38. Rajakrishnamoorthy, P.; Karthikeyan, D.; Saravanan, C.G. Emission reduction technique applied in SI engines exhaust by using zsm5 zeolite as catalysts synthesized from coal fly ash. *Mater. Today Proc.* **2020**, *22*, 499–506. [CrossRef]

39. Verrecchia, G.; Cafiero, L.; De Caprariis, B.; Dell'Era, A.; Pettiti, I.; Tuffi, R.; Scarsella, M. Study of the parameters of zeolites synthesis from coal fly ash in order to optimize their CO_2 adsorption. *Fuel* **2020**, *276*, 118041. [CrossRef]

40. Churata, R.; Almirón, J.; Vargas, M.; Tupayachy-Quispe, D.; Torres-Almirón, J.; Ortiz-Valdivia, Y.; Velasco, F. Study of Geopolymer Composites Based on Volcanic Ash, Fly Ash, Pozzolan, Metakaolin and Mining Tailing. *Buildings* **2022**, *12*, 1118. [CrossRef]

41. Vichaphund, S.; Aht-Ong, D.; Sricharoenchaikul, V.; Atong, D. Characteristic of fly ash derived-zeolite and its catalytic performance for fast pyrolysis of Jatropha waste. *Environ. Technol.* **2014**, *35*, 2254–2261. [CrossRef]

42. Ojha, K.; Pradhan, N.C.; Samanta, A.N. Zeolite from fly ash: Synthesis and characterization. *Bull. Mater. Sci.* **2004**, *27*, 555–564. [CrossRef]

43. Galindo Valbuena, H.M.; Medina, A.F.; Vargas, J.C.; Hernández Fandiño, O. Synthesis of zeolites Na-A, Na-X, and analcime from crushed stone waste and their applications in heavy metal removal in aqueous media. *Chem. Eng. Res. Des.* **2023**, *197*, 159–172. [CrossRef]

44. Jung, Y.J.; Kim, W.G.; Yoon, Y.; Kang, J.W.; Hong, Y.M.; Kim, H.W. Removal of amoxicillin by UV and UV/H_2O_2 processes. *Sci. Total Environ.* **2012**, *420*, 160–167. [CrossRef] [PubMed]

45. Znad, H.; Abbas, K.; Hena, S.; Awual, M.R. Synthesis a novel multilamellar mesoporous TiO_2/ZSM-5 for photo-catalytic degradation of methyl orange dye in aqueous media. *J. Environ. Chem. Eng.* **2018**, *6*, 218–227. [CrossRef]

46. Rodríguez Valdivia, M. Hydrothermal synthesis of zeolites from a volcanic ash by alkaline treatment and their potential application in the removal of NH_4^+, Pb^{2+}, Zn^{2+} and Mn^{2+}. *Matéria* **2022**, *27*, e13132. [CrossRef]

47. Novembre, D.; Gimeno, D. Synthesis and characterization of analcime (ANA) zeolite using a kaolinitic rock. *Sci. Rep.* **2021**, *11*, 13373. [CrossRef] [PubMed]

48. Vigil de la Villa Mencía, R.; Goiti, E.; Ocejo, M.; Giménez, R.G. Synthesis of zeolite type analcime from industrial wastes. *Microporous Mesoporous Mater.* **2020**, *293*, 109817. [CrossRef]

49. Setthaya, N.; Pindi, C.; Chindaprasirt, P.; Pimraksa, K. Synthesis of faujasite and analcime using of rice husk ashand metakaolin. *Adv. Mater. Res.* **2013**, *770*, 209–212. [CrossRef]

50. Jin, Y.; Qi, T.; Ge, Y.; Chen, J.; Liang, L.; Ju, J.; Zhao, J. Ultrasensitive electrochemical determination of phosphate in water by using hydrophilic TiO_2 modified glassy carbon electrodes. *Anal. Methods* **2021**, *13*, 996–1002. [CrossRef] [PubMed]

51. Jansson, I.; Suárez, S.; Garcia-Garcia, F.J.; Sánchez, B. Zeolite–TiO_2 hybrid composites for pollutant degradation in gas phase. *Appl. Catal. B* **2015**, *178*, 100–107. [CrossRef]

52. Katal, R.; Masudy-Panah, S.; Tanhaei, M.; Farahani, M.H.D.A.; Jiangyong, H. A review on the synthesis of the various types of anatase TiO_2 facets and their applications for photocatalysis. *Chem. Eng. J.* **2020**, *384*, 123384. [CrossRef]

53. Tayade, R.J.; Surolia, P.K.; Kulkarni, R.G.; Jasra, R.V. Photocatalytic degradation of dyes and organic contaminants in water using nanocrystalline anatase and rutile TiO_2. *Sci. Technol. Adv. Mater.* **2007**, *8*, 455–462. [CrossRef]

54. Dette, C.; Pérez-Osorio, M.A.; Kley, C.S.; Punke, P.; Patrick, C.E.; Jacobson, P.; Giustino, F.; Jung, S.J.; Kern, K. TiO_2 Anatase with a Bandgap in the Visible Region. *Nano Lett.* **2014**, *14*, 6533–6538. [CrossRef] [PubMed]

55. Shi, D.; Guo, Z.; Bedford, N. Nanotitanium Oxide as a Photocatalytic Material and its Application. In *Nanomaterials and Devices*; Elsevier: Amsterdam, The Netherlands, 2015; pp. 161–174. [CrossRef]

56. Dincer, I.; Zamfirescu, C. Hydrogen Production by Photonic Energy. In *Sustainable Hydrogen Production*; Elsevier: New York, NY, USA, 2016; pp. 309–391. [CrossRef]

57. Matsukawa, Y.; Hirata, S.; Inada, M.; Enomoto, N.; Hojo, J.; Hayashi, K. Kinetic effects of polymorphs and surface areas on adsorption and photocatalytic decomposition of acetaldehyde on titania. *Chem. Eng. J.* **2020**, *397*, 125422. [CrossRef]

58. Guo, B.; Shen, H.; Shu, K.; Zeng, Y.; Ning, W. The study of the relationship between pore structure and photocatalysis of mesoporous TiO_2. *J. Chem. Sci.* **2009**, *121*, 317–321. [CrossRef]

59. Labhane, P.K.; Patle, L.B.; Huse, V.R.; Sonawane, G.H.; Sonawane, S.H. Synthesis of reduced graphene oxide sheets decorated by zinc oxide nanoparticles: Crystallographic, optical, morphological and photocatalytic study. *Chem. Phys. Lett.* **2016**, *661*, 13–19. [CrossRef]

60. Sulaiman, F.; Sari, D.K.; Kustiningsih, I. The influence of ozone on the photocatalytic degradation of phenol using TiO_2 photocatalyst supported by Bayah natural zeolite. *AIP Conf. Proc.* **2017**, *1840*, 110014. [CrossRef]

61. Hunge, Y.M.; Yadav, A.A.; Kang, S.W.; Kim, H. Photocatalytic degradation of tetracycline antibiotics using hydrothermally synthesized two-dimensional molybdenum disulfide/titanium dioxide composites. *J. Colloid Interface Sci.* **2022**, *606*, 454–463. [CrossRef]